Cell

# The Mre11:Rad50 Structure Shows an ATP-Dependent Molecular Clamp in DNA Double-Strand Break Repair

Katja Lammens,[1,2,4] Derk J. Bemeleit,[2,4] Carolin Möckel,[2,4] Emanuel Clausing,[2] Alexandra Schele,[2] Sophia Hartung,[2] Christian B. Schiller,[2] Maria Lucas,[2] Christof Angermüller,[2] Johannes Söding,[2] Katja Sträßer,[1,2] and Karl-Peter Hopfner[1,2,3,*]

[1]Center for Integrated Protein Science Munich (CIPSM)
[2]Gene Center and Department of Biochemistry
[3]Munich Center for Advanced Photonics
Ludwig-Maximilians-University Munich, Feodor-Lynen-Strasse 25, 81377 Munich, Germany
[4]These authors contributed equally to this work
*Correspondence: hopfner@lmb.uni-muenchen.de
DOI 10.1016/j.cell.2011.02.038

## SUMMARY

The MR (*M*re11 nuclease and *R*ad50 ABC ATPase) complex is an evolutionarily conserved sensor for DNA double-strand breaks, highly genotoxic lesions linked to cancer development. MR can recognize and process DNA ends even if they are blocked and misfolded. To reveal its mechanism, we determined the crystal structure of the catalytic head of *Thermotoga maritima* MR and analyzed ATP-dependent conformational changes. MR adopts an open form with a central Mre11 nuclease dimer and two peripheral Rad50 molecules, a form suited for sensing obstructed breaks. The Mre11 C-terminal helix-loop-helix domain binds Rad50 and attaches flexibly to the nuclease domain, enabling large conformational changes. ATP binding to the two Rad50 subunits induces a rotation of the Mre11 helix-loop-helix and Rad50 coiled-coil domains, creating a clamp conformation with increased DNA-binding activity. The results suggest that MR is an ATP-controlled transient molecular clamp at DNA double-strand breaks.

## INTRODUCTION

DNA *d*ouble-strand *b*reaks (DSBs) are a major threat to genome stability in all kingdoms of life and can lead to gross chromosomal aberrations and cancer (Lee et al., 2008; Putnam et al., 2009; Wang et al., 2009). DSBs arise during chromosomal replication but can also be products of ionizing radiation and genotoxic chemicals (Costanzo et al., 2001; Ward, 1988). In addition, enzymatically induced DSBs are intermediates in V(D)J recombination, immunoglobulin class switching, and meiosis. Both sporadic and programmed DSBs need careful and prompt repair to maintain genome stability and allow cell survival.

DSBs elicit a complex cellular response and induce different repair pathways (Harper and Elledge, 2007). Repair proceeds predominantly by homologous recombination (HR), nonhomologous end joining (NHEJ), or microhomology-mediated end joining (MMEJ). In HR, DSBs are repaired error-free using the sister chromatid as template. In NHEJ, DNA ends are directly religated, often at microhomologies after limited, potentially mutagenic, processing of the DNA ends (MMEJ).

The central response factor for DSBs is the *M*re11:*R*ad50:*N*bs1 (MRN) complex (*M*re11:*R*ad50:*X*rs2 [MRX] in *Saccharomyces cerevisiae*). It is involved in most, if not all, DNA end-associated processes including damage checkpoint signaling, HR, NHEJ/MMEJ, telomere maintenance, and meiotic recombination (Borde, 2007; Lavin, 2007; Lee and Paull, 2007; Stracker et al., 2004; Williams et al., 2007). Hypomorphic mutations in human Mre11, Rad50, and Nbs1 are linked to the cancer predisposition diseases *N*ijmegen *b*reakage *s*yndrome (NBS), *A*taxia-*t*elangiectasia *l*ike *d*isorder (A-TLD), and NBS-like disorder (Carney et al., 1998; Petrini, 2000; Stewart et al., 1999; Varon et al., 1998).

The multifunctional MRN possesses both enzymatic and architectural activities. MRN activates the ATM kinase, resulting in activation and coordination of subsequent checkpoint and repair processes. The ATP-stimulated nuclease activity of MRN together with Sae2/CtIP then removes short oligonucleotides from the 5′ end of the DSBs (Budd and Campbell, 2009; Hopkins and Paull, 2008; Mimitou and Symington, 2008; Zhu et al., 2008). MRN additionally possesses a 3′–5′ exonuclease, ssDNA endonuclease and hairpin-opening activities, presumably to clean misfolded and blocked DNA ends (Paull and Gellert, 1998, 1999). Finally, MRN is implicated in tethering of DNA ends and chromatids via coiled-coil tails of Rad50 (Hopfner et al., 2002).

Homologs for Mre11 and Rad50, but not Nbs1, are found in all three phylogenetic domains and are also known as SbcC (Rad50 homolog) and SbcD (Mre11 homolog) in bacteria (Sharples and Leach, 1995). The prokaryotic MR complex shares enzymatic activities and morphological features with eukaryotic MRN and is implicated in processing and repair of DNA double-strand

breaks, interstrand crosslinks, and replication fork-associated hairpins (Bentchikou et al., 2007; Cromie et al., 2001; Eykelenboom et al., 2008; Leach et al., 1997; Mascarenhas et al., 2006; Zahradka et al., 2009). MR is a large, bipolar complex containing two Mre11 and two Rad50 polypeptides (Hopfner et al., 2001). The Mre11 dimer and the two Rad50 nucleotide-binding domains (NBDs) form a ''catalytic head'' that harbors ATP-stimulated nuclease and DNA-binding activities. Two long Rad50 coiled-coil domains protrude from this head and can bind other MR complexes via their apical zinc-hook dimerization motifs (de Jager et al., 2001; Hopfner et al., 2002), thereby forming large molecular bridges to transiently tether broken chromosomes (Lobachev et al., 2004).

The functional interplay of Rad50s ATPase and the Mre11 nuclease in DSB repair remained unclear, mostly because there is not a structural framework for the catalytic head complex. As a consequence, the role of Rad50s ATPase function has been unclear, although it is essential for MR(N/X) function (Bhaskara et al., 2007). Likewise, it is unknown why DSB recognition by MR(N/X) has no clear biochemical preference for DNA ends or hairpins and binds DNA also at internal sites. This is important because MRN can sense and clear protein-bound DNA ends in vitro (Connelly et al., 2003) and in vivo (Lobachev et al., 2002; Neale et al., 2005). The remarkable ability to clean up blocked and misfolded ends using an ATP-driven nuclease activity distinguishes MR(N/X) from, e.g., the NHEJ protein Ku (Walker et al., 2001).

To provide a structural framework for the complex between Mre11 and Rad50, we determined the X-ray crystal structure of the catalytic head of the *Thermotoga maritima* MR (SbcCD) complex as well as the crystal structure of the AMPPNP-bound Rad50 NBD dimer in complex with the Rad50-binding helix-loop-helix motif (HLH) of Mre11. We also analyzed ATP-dependent conformational changes of the MR head module by *s*mall-*a*ngle *X*-ray *s*cattering (SAXS) and chemical crosslinking assays. The structure revealed that Mre11 and Rad50 form a large ATP controlled molecular clamp, suited to recognize even blocked DSBs. The observed interfaces were tested by mutating homologous regions in eukaryotic MRX in *Saccharomyces cerevisiae*. Finally, we demonstrate that ATP binding to Rad50 induces conformational changes in the Mre11 dimer, providing a mechanistic role for Rad50s ATP-binding activity in controlling DNA processing by Mre11. This unifies the functional architecture of MR with other ABC type molecular machines such as ABC transporters.

## RESULTS AND DISCUSSION

### Structure Determination

We copurified and crystallized Mre11 from *Thermotoga maritima* (*Tm*) and a shortened Rad50 (see Experimental Procedures) that comprises the *n*ucleotide-*b*inding *d*omain (NBD) and approximately 50 amino acids of the Mre11-binding coiled coil ($Rad50^{NBD}$). The two ends of the shortened coiled coil are fused by a short linker. Both proteins form a stoichiometric complex with ATPase as well as DNA-binding activity (see Figure S1 available online). Crystals of space group I222 contained one full catalytic head ($M_2$:$R^{NBD}{}_2$) per asymmetric unit and diffracted X-rays to 3.4 Å resolution. Single wavelength anomalous dispersion phasing and density modification produced an interpretable electron density for both Mre11s and one $Rad50^{NBD}$ (Figure 1A). Electron density for the second Rad50 was less defined, presumably because this domain is more mobile due to lack of additional crystal contacts. However, we could rigid-body dock the model obtained from the well-defined $Rad50^{NBD}$ into the density of the second $Rad50^{NBD}$ using unambiguous anomalous difference density markers and some secondary electron density. Both $Rad50^{NBD}$s interact with Mre11 in a similar manner. The resulting $M_2$:$R^{NBD}{}_2$ heterotetramer could be refined with acceptable geometry and R values (Table S1).

### Crystal Structure of the Bacterial Mre11:Rad50 Catalytic Head

The *Tm*MR catalytic head (*Tm*$MR^{NBD}$) is an elongated crescent shaped complex with approximately 60 × 70 × 210 Å dimensions (Figures 1A and 1B). Its core is formed by a dimer of the two Mre11 nuclease domains, with the two nuclease-active sites located near the center of the concave face. The Rad50 NBDs each attach to the outside of the nuclease dimer and form the tips of the crescent. The Rad50 coiled coils protrude from the convex side of the catalytic head, opposite to the nuclease-active sites, at an angle of approximately 120° from each other. This architecture fits well the bipolar shapes of full prokaryotic MR and eukaryotic MRN complexes previously visualized by electron and scanning force microscopy (Connelly et al., 1998; de Jager et al., 2001; Hopfner et al., 2001).

The NBDs of Rad50 possess the typical bilobed ABC fold, whereas Mre11 shows an extended structure, composed of two functional modules, the ''nuclease module'' and the Rad50-binding domain. The nuclease module comprises the phosphodiesterase and accessory DNA-binding ''capping'' domains. The Rad50-binding domain contains a helix-loop-helix (HLH) domain that binds to the root of Rad50s coiled coil. Surprisingly, the nuclease module and the HLH domain are widely separated and connected by a long, poorly structured linker, that wraps around Rad50s NBD and places the capping and HLH domains of Mre11 on opposite sites of it. A second interaction is formed between Mre11's capping domain and Lobe II of Rad50s NBDs, stabilizing the observed extended domain arrangement between Mre11 and Rad50 in the catalytic head.

To verify the domain arrangements found in the crystal structure, we performed small-angle X-ray scattering (SAXS). The experimentally derived SAXS intensities of $MR^{NBD}$ closely match the scattering intensities calculated from its crystal structure and individual as well as averaged ab initio SAXS models exhibit the elongated shape of the atomic model (Figures 1C and 1D). This supports the conclusion that the MR crystal structure we present here closely resembles the conformation of the complex in solution.

The overall structure explains two poorly understood functional characteristics of MR. The widely separated, outward placement of the Rad50 NBDs allows unobstructed access of DNA to the Mre11 active sites, even if DNA ends are blocked by large proteins. In addition, our structure shows that the complex has the potential to undergo major conformational changes, consistent with the observation of large conformational

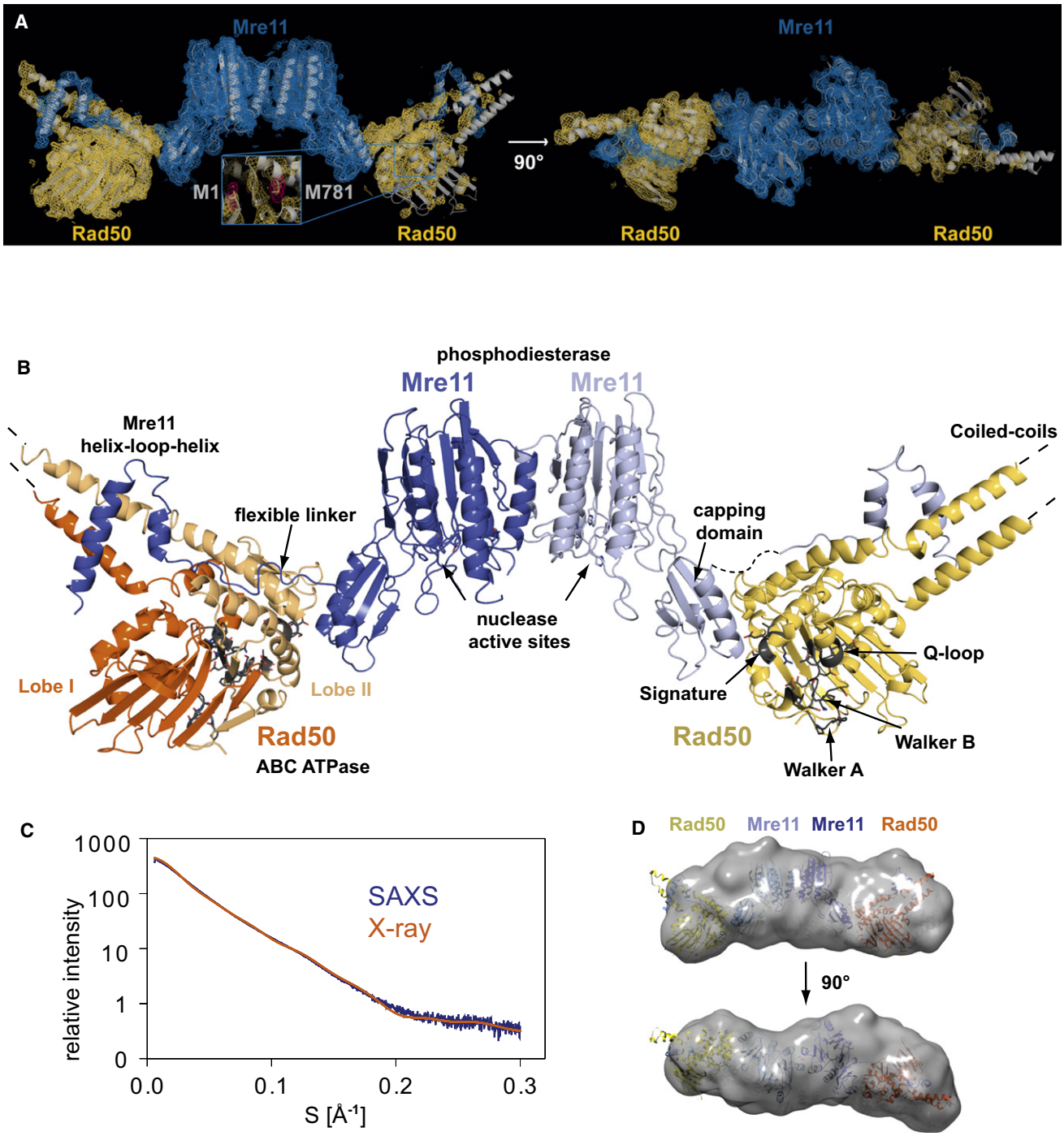


**Figure 1. Overall Structure of the Crescent-Shaped Mre11:Rad50 Catalytic Head**

(A) Experimental electron density map (contoured at 1.0 σ and colored blue for Mre11 and yellow for Rad50) superimposed with a ribbon representation of the *Thermotoga maritima* Mre11:Rad50$^{NBD}$ complex (gray). Two views are shown. Inset: anomalous difference electron density map for the selenium atoms (pink, contoured at 5.0 σ).

(B) Ribbon representation of the bacterial Mre11 Rad50 catalytic head. Individual domains and important motifs are highlighted and annotated.

(C) Experimental small-angle X-ray scattering (SAXS) profile (blue) compared with the theoretical scattering curve calculated from the crystal structure of the complex (orange).

(D) Two orthogonal views of the average SAXS envelope of the Mre11:Rad50$^{NBD}$ assemblies (calculated with DAMMIN, the atomic model of the complex) highlight the similarity of crystal structure and solution conformation.

See also Figure S1 and Table S1.

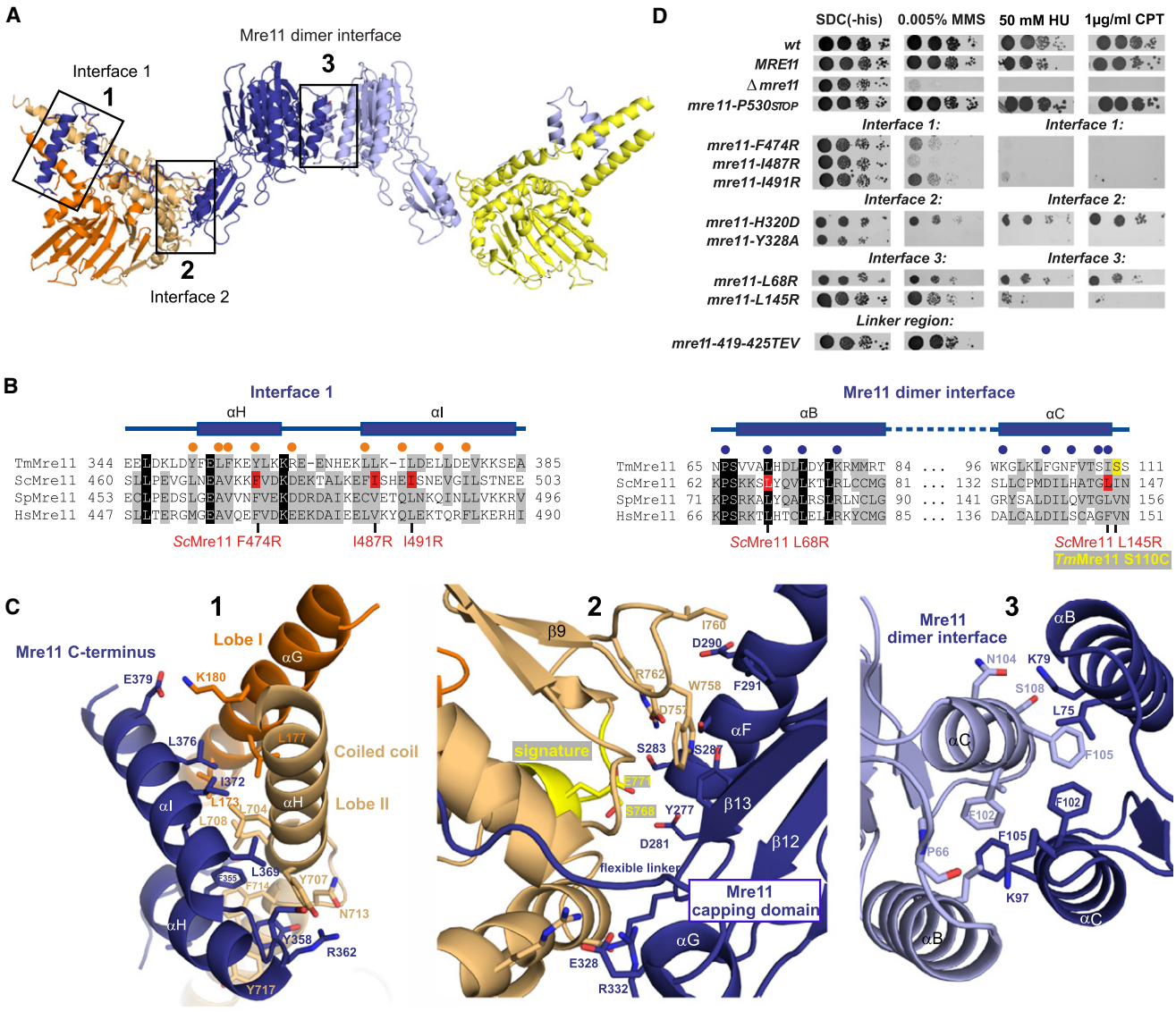


**Figure 2. Details of Mre11:Rad50$^{NBD}$ and the Mre11 Dimer Interfaces**

(A) Ribbon representation of the Mre11:Rad50$^{NBD}$ complex colored according to Figure 1B. The boxed interfaces (1, 2, 3) are shown in (C).

(B) Sequence alignment of the Mre11 HLH domain (αH and αI) and the Mre11 dimer interface (αB and αC). Yeast mutations analyzed in (D) are highlighted in red. Spheres represent residues implicated in Mre11$^{HLH}$:Rad50$^{NBD}$ (orange) and Mre11:Mre11 interaction (blue).

(C) Details of macromolecular interfaces. Selected side chains are shown as color-coded sticks and are annotated. (1) The Mre11 helix-loop-helix (HLH) motif (blue) and its interaction with the base of the Rad50 coiled coil (orange and yellow). (2) The interface between the capping domain of Mre11 (blue) and the opposite Rad50 (orange) region in close proximity to the signature motif (yellow). (3) The Mre11 dimerization interface.

(D) Yeast survival assays by serial dilutions show that mutations in Mre11 predicted to affect interface 3 (L145R, L68R), mutations within the helix-loop-helix motif predicted to affect interface 1 (L474R, I487R, I491R), and mutations in the capping domain predicted to affect interface 2 (H320D, Y328A) result in sensitivity to methyl-methanesulfonate (MMS), hydroxyurea (HU) and camptothecin (CPT). Changing the flexible linker residues (419-425 TEV) has no strong effect on MMS sensitivity. Left: SDC medium without histidine alone. Right: media supplemented with indicated concentrations of MMS, HU, or CPT.

See also Figure S2.

changes identified by scanning force microscopy of human MRN (Moreno-Herrero et al., 2005).

## Details of Mre11:Rad50 Interfaces

There are three types of macromolecular interfaces in MR$^{NBD}$, one between the two Mre11 subunits and two between Mre11 and Rad50 (Figures 2A–2C). A fourth interface between the two Rad50 NBDs in the presence of ATP will be described below. The two Mre11 phosphodiesterase domains interact by forming a four-helix bundle (αB and αC from both protomers) around central hydrophobic/aromatic residues (F102, F105, and L75 from both protomers) (Figure 2C3). This interface is related to

that seen in the crystal structure of the catalytic domain of *P. furiosus* Mre11, showing that the architectural principles of MR are conserved.

Rad50 binds Mre11 with two interfaces (1 and 2) comprising areas of 1334 and 686 Å$^2$, respectively. Interface 1 (Figures 2A–2C) is formed by binding of the Mre11 C-terminal HLH domain to the coiled-coil root of Rad50, with αH and αI of the HLH domain binding perpendicularly across Rad50s coiled coil. αH$^{Mre11}$ binds only one coiled-coil helix (αH$^{Rad50}$), whereas αI$^{Mre11}$ reaches across both coiled-coil helices (αG$^{Rad50}$ and αH$^{Rad50}$). Interestingly, αH$^{Mre11}$ binds to αH$^{Rad50}$ at a pronounced kink and extended loop, located directly opposite the start of αG$^{Rad50}$ at the other side of the coiled coil. Thus, the coiled coil is attached to the NBD not with a continuous helix, but with a structure that may allow for movements between the coiled coil and Mre11-binding site and the globular part of the ATPase.

The HLH motif and coiled-coil domains bind to each other via an array of aromatic and hydrophobic residues. αH$^{Mre11}$ and αH$^{Rad50}$ interact through eight aromatic residues (Mre11: Y351, F352, F355, Y358; Rad50: Y707, F714, Y717, F718). The interface is further stabilized mainly by hydrophobic interactions between αI$^{Mre11}$ and αG$^{Rad50}$ but also some specific hydrogen bonds and salt bridges, e.g., between E379$^{Mre11}$ and K180$^{Rad50}$ (Figure 2C).

The linker preceding αH$^{Mre11}$ and connecting the HLH domain with the nuclease module runs along the outside of the NBD at Lobe II until it reaches the capping domain at the second interface between Rad50 and Mre11. Although parts of the linker adjacent to the HLH domain are ordered and we observe a few, dispersed hydrophobic and ionic contacts to the NBD, some parts appear to be disordered, suggesting that the linker acts as a flexible leash.

Interface 2 (Figure 2C) is formed between one face of Mre11's capping domain and the "bottom" side of Rad50s Lobe II (the side opposite the coiled coil). This interface is predominantly polar, although W758$^{Rad50}$ and I760$^{Rad50}$ bind a small hydrophobic patch at the core of this interface (F291$^{Mre11}$), located at the edge of the β sheet of the capping domain, with contributions from the flanking αF$^{Mre11}$. Interestingly, a part of the interface is mediated by the signature motif, which becomes bound by ATP in the engaged conformation of the NBDs. Likewise, the Mre11 capping domain also participates in DNA binding (Williams et al., 2008). Consequently, interface 2 could transiently stabilize the "open" conformation with separated NBDs until DNA and/or ATP is bound while also allowing the NBDs mobility for ATP-induced conformational changes (see below).

## Mutational Analysis of Mre11:Rad50 Interfaces in *S. cerevisiae* In Vivo

To verify the functional significance of the observed interfaces in vivo, we tested mutants in all three interfaces of *Saccharomyces cerevisiae* MRX for their ability to complement the methyl methanesulfonate (MMS), hydroxyurea (HU), and camptothecin (CPT) sensitivity of the *Δmre11* strain (Figure 2D). Mutations were chosen on the basis of sequence conservation (Figure 2B) or using a structure of *S. pombe* Mre11 as guide (unpublished data). We also tested a replacement of seven residues of the linker between catalytic and Rad50-binding domains of Mre11 with a TEV protease target sequence (419-425TEV) and a Mre11 truncation variant (P530STOP). All proteins were expressed at normal levels according to western blot analysis (Figure S2). Consistent with previous data, wild-type *MRE11* and the *mre11-P530STOP* (resulting in a protein truncated after the HLH region) confers resistance to MMS, HU, and CPT in the *Δmre11* strain (Chamankhah and Xiao, 1999). The Mre11 dimer interface mutants (L145R and L68R) can only partially rescue MMS, HU, and CPT sensitivity, similar to what has been observed in the case of *S. pombe* Rad32 (Williams et al., 2008). In addition, we found that F474R, I487R, and I491R in Mre11:Rad50 interface 1 (HLH$^{Mre11}$:coiled coil$^{Rad50}$) do not rescue MMS, HU, and CPT sensitivity. Finally, the Mre11:Rad50 interface 2 (Cap$^{Mre11}$:NBD$^{Rad50}$) mutations H320D and Y328A partially or completely fail to rescue MMS, HU, and CPT sensitivity. Previously, it was found that an 11 amino acid deletion mutant of the *S. cerevisiae* Mre11 at the predicted interface 2 (Mre11-6) also shows MMS sensitivity and DSB processing defects (Usui et al., 1998).

In contrast, *mre11 419-425TEV* complements the *Δmre11* strain. This indicates that the sequence of the "linker" region is not important for the activity of MRX on homologous recombination. Coexpression of TEV protease did not result in significantly increased MMS sensitivity, although most Mre11 was cleaved, according to western blot analysis (data not shown). It is possible that low levels of residual or newly synthesized Mre11 are sufficient to complement MMS sensitivity. In support of this, coexpression of the catalytic and Rad50-binding domains of *S. cerevisiae* Mre11 could not complement *Δmre11* (data not shown). In summary, all observed interfaces of *Tm*MR$^{NBD}$ are functionally significant for the yeast MRX complex in vivo.

## ATP- and DNA-Induced Engagement of Rad50 NBDs

Because ATP hydrolysis by Rad50$^{NBD}$ requires formation of a tightly engaged NBD dimer with sandwiched ATP molecules (Hopfner et al., 2000) (Figure 3A), we recorded SAXS intensities of *Tm*MR$^{NBD}$ in the absence and presence of ATPγS to test whether NBDs from a single head engage by a large conformational change, or alternatively NBDs from different heads assemble in the presence of ATP (Figure 3B). Adding ATPγS indeed resulted in a substantial decrease of the radius of gyration ($R_g$) from 230 to 193 Å as well as a more pronounced peak at shorter vectors and a significant decrease of the long vectors in the pair distribution function P(R) (Figure 3B). Thus, ATPγS renders the complex more compact, consistent with an expected engagement of the two NBDs within a single catalytic head, but not with ATP-mediated clustering of multiple MR catalytic heads.

Although ATPγS induces a compact conformation, the residual long vectors in P(R) indicate that the population still contains a substantial amount of the open form. Attempts to obtain a more homogeneous population by addition of various amounts of ATPγS, or AMPPNP, ADP plus $BeF_3$ or $AlF_3^-$ or using a Walker B E798Q mutation in combination with ATP, have been unsuccessful.

We therefore investigated the ATP-dependent engagement of the two Rad50 NBDs by site-specific crosslinking. We

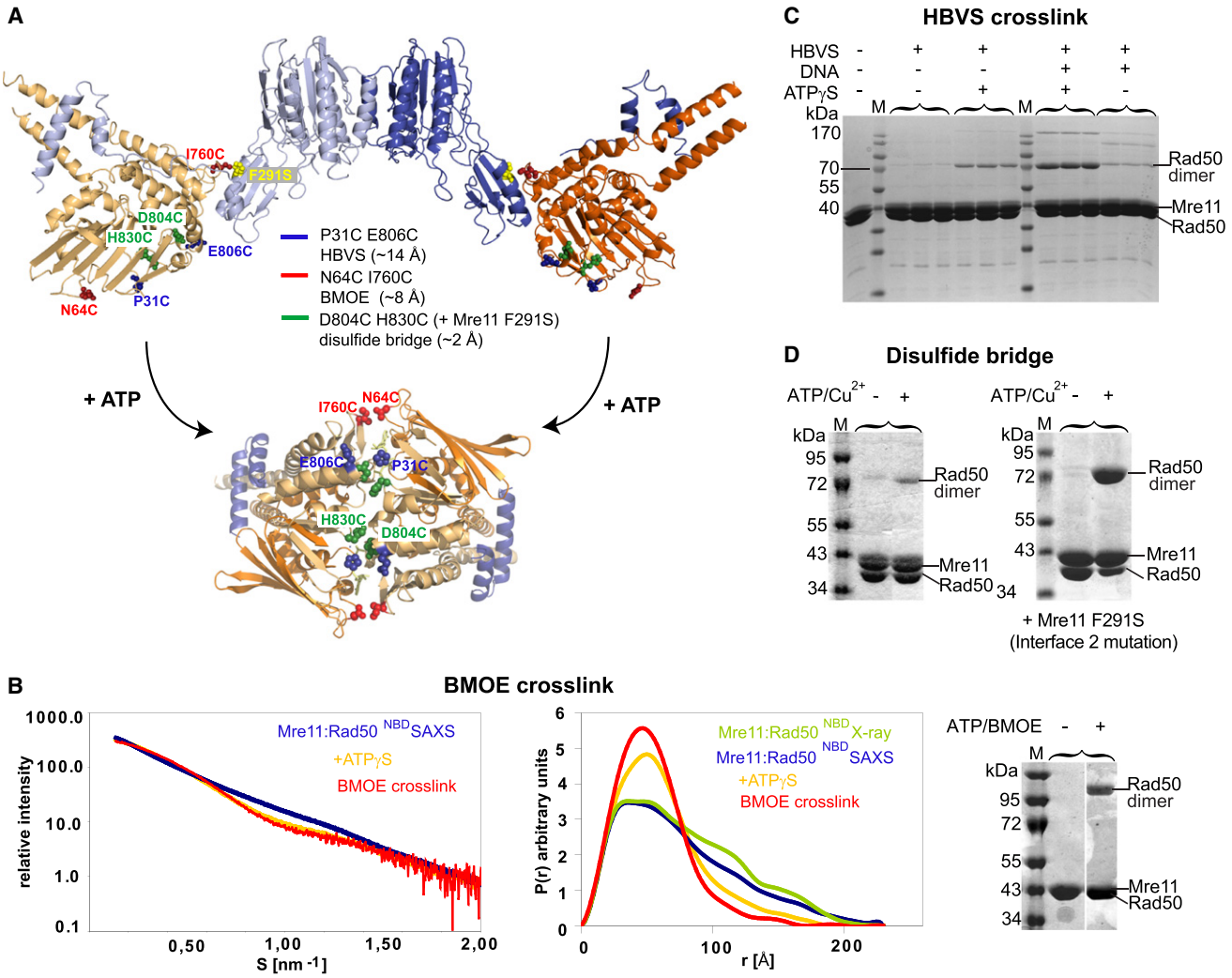


**Figure 3. ATP Engages Rad50$^{NBD}$s in the Catalytic Head**

(A) Cysteine mutations introduced in *Tm*Rad50$^{NBD}$ to test formation of the ATP-bound Rad50 dimer. Sites are widely separated in the open form (upper crystal structure), but closely spaced for crosslinking or disulfide bonding in the ATP-bound form (below, see Figure 4).

(B) Left panel: Superposition of experimental SAXS curves of Mre11:Rad50$^{NBD}$ with and without ATPγS indicates a more compact, globular shape in the presence of ATPγS. SAXS of the BMOE crosslinked Mre11:Rad50$^{NBD,N64C,I760C}$ results in a shape similar to the ATPγS-bound form. Middle panel: the electron pair distance distribution function P(r) in the absence of nucleotides corresponds well to the crystal structure derived P(r). ATPγS increases the short distances and decreases the long distances. Residual long distances suggest a heterogeneous mixture between the open form and closed ATPγS complex. The BMOE crosslinked complex has a similar shape to the ATPγS complex but appears to be more homogenous for the compact form. Right panel: Nonreducing Coomassie stained SDS-PAGE of the MR$^{NBD,N64C,I760C}$ crosslinking experiment using BMOE. The crosslinking forms a covalently connected Rad50 dimer in an ATP-dependent manner.

(C) Chemical crosslinking by HBVS of MR$^{NBD,P31C,E806C}$ creates a covalently connected Rad50 dimer in an ATPγS and DNA-dependent manner. The identity of the corresponding gel band was confirmed by mass spectrometry.

(D) The formation of ATP-bound engaged Rad50$^{NBD,D804C,H830C}$ is tested by using ATP/$Cu^{2+}$-dependent disulfide bond formation. Modulating the Mre11:Rad50 interface 2 by Mre11$^{F291S}$ results in dramatically increased disulfide bond formation efficiency, consistent with the idea that interface 2 stabilizes the open form and is disrupted in the closed form.

See also Figure S3.

engineered three pairs of suitable cysteine residues at positions that are predicted to be far apart in the nucleotide free form but close together in the ATP-bound dimer of Rad50$^{NBD}$ (Figure 3A). P31C plus E806C were introduced to allow crosslinking analysis by the thiol reactive agent 1,6-Hexane-bis-vinylsulfone (HBVS). Although 110 Å apart in the open form, their estimated distance of 10 Å in the closed form matches the range of HBVS. In the absence of ATPγS and DNA, we do not see substantial crosslinking, in agreement with the large separation of the two NBDs (Figure 3C). However, ATPγS increases the crosslinking efficiency. The composition of the crosslinked species was verified by mass spectrometry. We also observe some increased

crosslinking efficiency in the presence of plasmid DNA, suggesting that DNA has an influence on the NBD arrangement. Some additional bands arise presumably from nonspecific crosslinking. Significantly, the crosslinking efficiency substantially increases further in the presence of both ATPγS and DNA, suggesting that ATP and DNA cooperate in forming the engaged NBD form. Gel filtration or SAXS on the crosslinked species never revealed evidence of higher-molecular-weight complexes, ruling out crosslinking of adjacent MR complexes on DNA (Figure S3A).

Although the low to moderate crosslinking efficiency (10%–20%) of the HBVS crosslinker enables detection of allosteric effects of DNA addition, it is not suited to analyze the structural and biochemical properties of the crosslinked protein. Using I760C plus N64C (approximately 110 Å apart in the nucleotide free form but approximately 8 Å apart in the ATP-bound form), we could very efficiently (up to 70%) crosslink the two NBDs in the presence of ATP, but not in the absence of ATP (Figure 3B, right panel and Figure 3D). This independently verifies the clamping movement of the NBDs. The proposed clamp movement can also be seen by ATP-induced formation of a disulfide bond between D804C and H830C, which are ideally positioned at opposite interface loops in the ATP-bound form of NBDs (Figure 3D). The high efficiency of I760C/N64C in the presence of BMOE compared to the disulfide bond could possibly arise from the fact that $I760^{Rad50}$ is located in interface 2. If interface 2 stabilizes the open form, as seen in the crystal structure, the prediction is that destabilizing interface 2 will increase the efficiency of formation of the closed form. To test this idea, we introduced F291S ($F291^{Mre11}$ interacts with $I760^{Rad50}$ in interface 2) into Mre11 and analyzed disulfide bond formation (Figure 3D). Consistently, although still no efficient disulfide bond formation is observed in the absence of ATP, we can now efficiently crosslink the NBDs by disulfide bond formation. This is corroborated by a slight, but statistical significant increase in ATP hydrolysis activity of the mutants that disrupt interface 2 (Figure S3G).

To see whether the crosslinked protein has a structure similar to the ATP-bound protein, we prepared BMOE crosslinked protein in the presence of ATP (about 65% crosslinked) and purified the crosslinked species by gel filtration to remove ATP. This step also enriched the crosslinked species, and we thus performed SAXS. Indeed, the solution structure of the crosslinked protein is very similar to the ATPγS-bound protein (Figure 3B), validating the idea that the crosslink stabilizes the closed conformation. We conclude that ATPγS induces a conformation in MR's catalytic head with engaged NBDs, thereby the transient interface 2 is disrupted. Besides forming interface 2, the Mre11 capping domains are also involved in DNA binding (Williams et al., 2008). This favors a model in which DNA allosterically helps to modulate interface 2, thus explaining why it promotes formation of the closed state.

To analyze whether the closed $MR^{NBD}$ structure is formed around DNA, we performed the HBVS crosslinking and disulfide bridging in the presence of single-stranded and/or double-stranded plasmid DNA (pBSII KS+, ΦX174 Virion and ΦX174 RF II) under conditions where in EMSA most of the DNA is shifted by bound protein (Figures S3A–S3F). In all cases, subsequent gel filtration failed to detect comigrating DNA and protein; i.e., the protein is not crosslinked around internal DNA.

## ATP-Bound Rad50 NBDs in Complex with Mre11

We crystallized *Tm*$Rad50^{NBD}$ in complex with the *Tm*Mre11 HLH domain (residues 343–385) in the presence of the nonhydrolyzable ATP analog adenylyl-imidodiphosphate (AMPPNP) (Figure 4A; Figure S4; Table S2). Although the archaeal Rad50 ATPase domain has been crystallized as ATP-bound dimer before (Hopfner et al., 2000), this structure lacked the coiled-coil domain and could not give insights into how ATP might impact on the orientation of the coiled-coil domain and Mre11 interaction.

The AMPPNP-bound structure was determined to a resolution of 1.9 Å and offers a much more detailed view of nucleotide coordination and hydrolysis (Figures 4B and 4C). The Walker A motifs bind the three phosphates of the AMPPNP moieties, whereas the Signature motifs of the opposing NBDs coordinates the γ-phosphates. $Mg^{2+}$ is coordinated by oxygens from β and γ phosphate, two water molecules and side chain oxygens of S37 (Walker A) and Q142 (Q loop). A bound water molecule (W1) is suitably located for nucleophilic attack on the γ-phosphate, positioned, and activated by hydrogen bonds to E798 (Walker B), H830 (His-switch), and the main chain oxygen of S802 (opposing D loop) (Figure 4C). In addition, the helix following the Q loop and the subsequent coiled-coiled domains are nicely visualized and well ordered, allowing comparison of nucleotide-bound and -free states of the interaction site between Mre11 and Rad50 (Figures 4D and 4E).

ATP binding not only tightly engages the two NBDs but induces a second conformational change within the NBDs, resulting in an approximately 50° rotation of the Signature motif helix (Figure 4E) with respect to the Walker motifs. This rotation is the result of Q142 (Q loop) binding to $Mg^{2+}$, inducing a conformation within the NBDs that enables tight NBD-NBD engagement. As a consequence, the coiled coil and the interacting HLH domain of Mre11 undergo a "rigid-body" rotation by approximately 50° with respect to ATP binding Lobe I.

Formation of the engaged NBDs strongly affects the angle between the two coiled coils protruding from the DNA-binding catalytic head, consistent with scanning force microscopy of human MRN (Moreno-Herrero et al., 2005), where DNA binding was shown to alter the angle between two coiled coils of about 60°. Comparing the angle between coiled coils in the "open" conformation (~120°) and the ATP-bound "closed" state (~60°), we also see a difference of about 60°. Our data therefore suggest that the identified clamp movement in the catalytic head is the molecular basis for the observed mesoscale movements of the MRN coiled coils upon DNA binding. We envision that DNA binding to the capping domains of Mre11 help to displace the NBDs from interface 2, allowing them to adopt a closed conformation in the presence of ATP.

## Rad50 Induces a Conformational Change in the Mre11 Dimer

The NBDs within a single MR catalytic head undergo an engagement-disengagement cycle similar to that seen in ABC transporter (Hollenstein et al., 2007; Oldham et al., 2008). In ABC

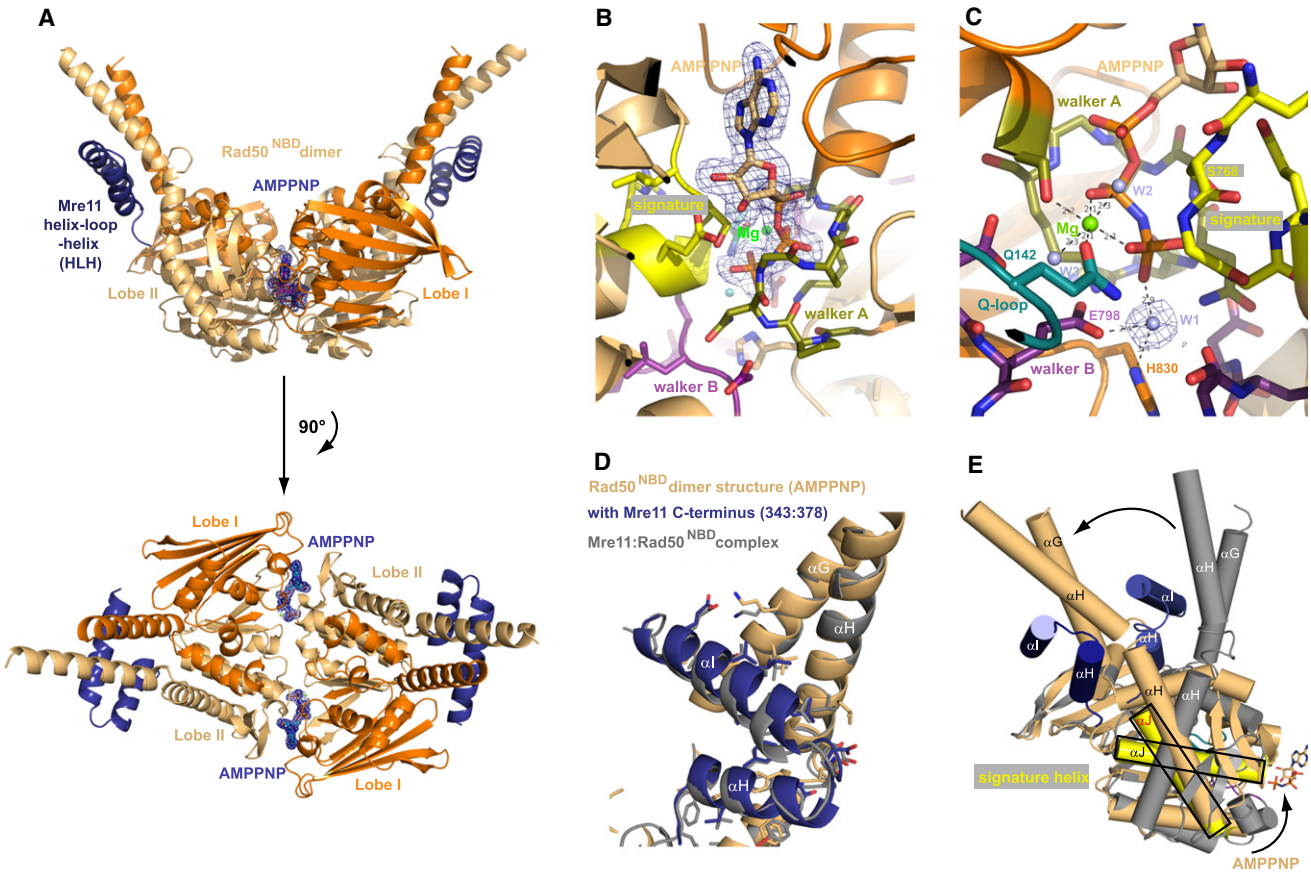


**Figure 4. Structure of the AMPPNP-Bound Rad50$^{NBD}$ Dimer in Complex with the HLH Domain of Mre11**

(A) Two perpendicular views of a ribbon representation of the AMPPNP-bound Rad50$^{NBD}$ dimer in complex with the C-terminal helix-loop-helix region of Mre11 color coded according to Figure 1B. AMPPNP is highlighted and shown with 2FoFc electron density (1σ contour).

(B and C) Two views of the ATP-binding site with $2F_o$-$F_c$ electron density around AMPPNP (B) or the nucleophilic water ("W1" in C) and highlighted and color-coded ATP-binding motifs signature motif (yellow), Walker A (olive), Walker B (purple), Q loop (turquoise), and $Mg^{2+}$ ion (green sphere).

(D) Superposition of Rad50$^{NBD}$ from apo (from MR catalytic head, gray) and AMPPNP (blue/orange) crystal structures at Lobes II shows that for *T. maritima* MR, coiled-coil structure and interaction interface 1 are not directly modulated by AMPPNP binding.

(E) Superposition of apo and AMPPNP-bound forms of Rad50$^{NBD}$s via Lobe I shows that AMPPNP binding induces a large, approximately 50° rotation between Lobe I and Lobe II, leading to a rigid-body movement (arrow) of the HLH and coiled coil with respect to the ATP-binding interface of Rad50.

See also Figure S4 and Table S2.

transporter, ATP-dependent NBD engagement drives conformational changes in transmembrane domains (TMDs), a "power-stroke" that transports solutes across the membrane. To see whether Rad50 ATP binding can alter the Mre11 dimer, in analogy to the function of NBDs in ABC transporter, we tested the conformation of the Mre11 dimer using a crosslinking approach. In support of such a function, the "angles" between Mre11 protomers in *T. maritima* and *P. furiosus* Mre11 dimers are quite different and the *Tm*Mre11 dimer needs to undergo a pivoting rotation to be able to bind DNA similar to the *Pf*Mre11 nuclease dimer (Figure 5A) (Williams et al., 2008).

We mutated Mre11 dimer interface residues S110 in *Tm*Mre11 and F102 in the *Pf*Mre11 to cysteines. The introduced cysteines in both protomers are separated by approximately 6–8 Å, close enough to be able to form a disulfide bond or be substrates for BMOE (8 Å) in a manner that might be sensitive to changes in the Mre11 dimer. Both mutants form $M_2R_2^{NBD}$ heterotetramers and otherwise behave like wild-type protein during purification, and the Mre11 interface is not physically disrupted. Indeed, the cysteine-engineered Mre11s could be efficiently crosslinked with either BMOE or by forming disulfide bonds (Figures 5C–5F), whereas the longer HBVS crosslinker did not efficiently crosslink Mre11 (data not shown).

ATP, AMPPNP, and ATPγS reduced the ability of BMOE to crosslink Mre11 S110C dimers in MR$^{NBD}$ up to approximately 50%, and the most plausible explanation is that the structure of the Mre11 dimer is altered such that the position of the opposing engineered cysteines is changed. As control, ADP did not reduce but seems to slightly increase crosslink efficiency as if stabilizing a different conformation than ATP. DNA did not largely impact on the crosslinking efficiency but perhaps DNA-induced changes that are not sensitive to our method (Figure 5E). To rule out crosslinker-specific effects, we also tested the formation of a disulfide bond. Whereas *Tm*MR$^{S110C}$ formed

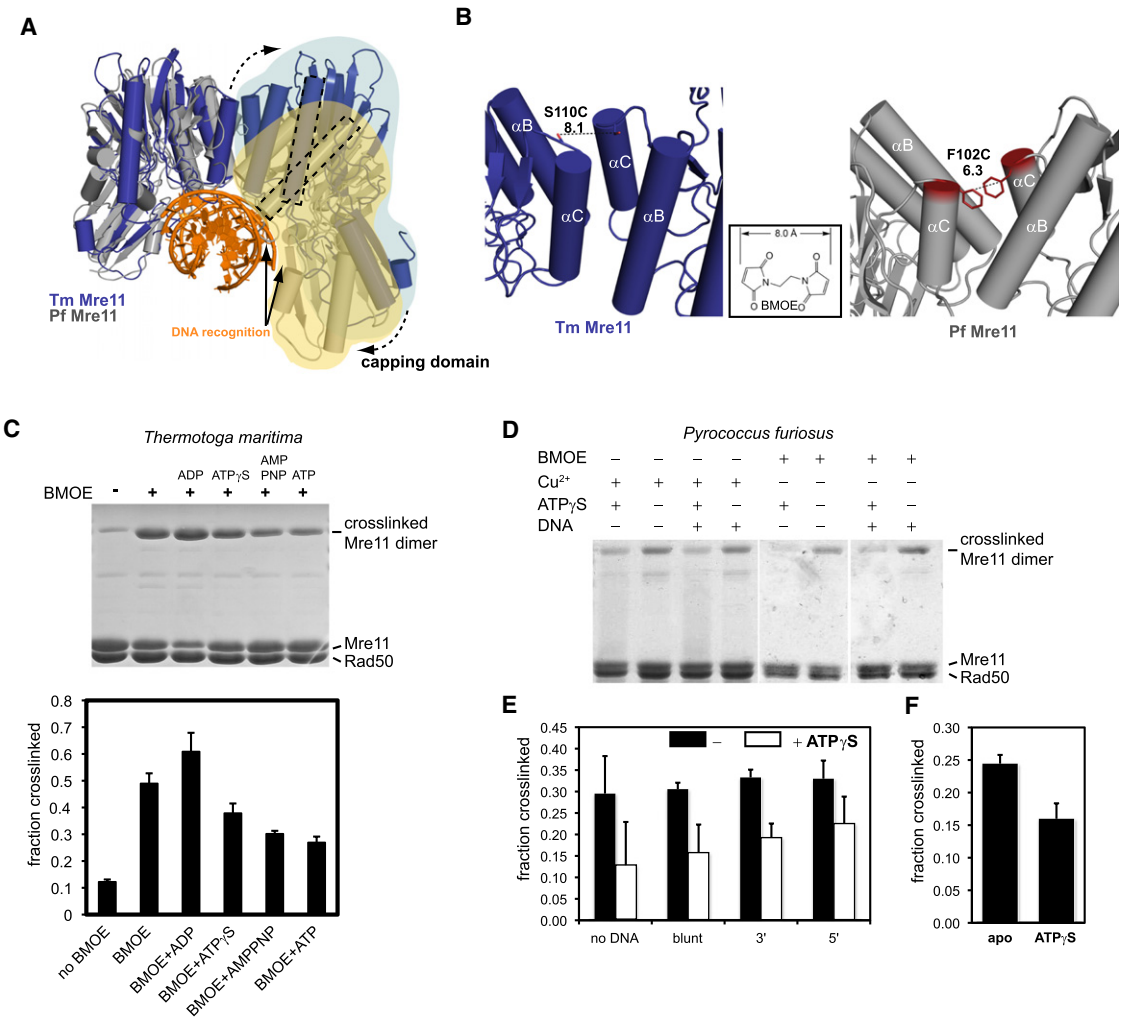


**Figure 5. ATP Binding to Rad50 Changes the Mre11 Dimer Interface**

(A) Comparison of the nuclease dimer of DNA-bound *Pf*Mre11 (gray, yellow, orange) with that of *Tm*Mre11 (blue, light blue). Both complexes are superimposed via the left protomer. In *T. maritima,* the right protomer has to undergo a substantial rigid-body motion to adopt the same DNA-binding contacts (solid arrows) and conformation as seen for *Pf*Mre11 (dashed arrow). This can be seen by the different orientations of the minor groove binding helix (dashed rectangles).

(B) To probe for conformational changes, we mutated S110C in *Tm*Mre11 (left panel) and F102C in *Pf*Mre11 at a position that is expected to undergo movements when switching between different pivot angles. The distances are suitable for crosslinking with a short bifunctional sulfhydryl directed crosslinker (inset: BMOE), or by forming disulfide bonds.

(C) Crosslinking analysis of *Tm*Mre11 dimer structure. Upper panel, nonreducing Coomassie-stained SDS-PAGE of *Tm*MR$^{NBD}$ crosslinked under different conditions (lane labels see lower panel); lower panel, quantification of the crosslinking efficiency (mean ± standard deviation [SD] of three independent experiments) for different conditions and adenosine nucleotides. A crosslinked band corresponding to the Mre11 dimer in the absence of BMOE crosslinker indicates disulfide bond formation.

(D) Coomassie-stained nonreducing SDS-PAGE of crosslinked *Pf*MR$^{NBD}$, showing different conditions and replicates. $Cu^{2+}$ was used to increase disulfide bond formation.

(E and F) Quantification of crosslinking efficiency by BMOE (E) or disulfide bonds (F). Error bars depict standard deviations. In (F), the effect of ATPγS is tested. In (E), the effect of dsDNA 50 mer with either blunt ends or 3′ or 5′ 10 dT ssDNA overhangs is shown. Black bars are without ATPγS, white bars with ATPγS.

disulfide bonds already during purification (Figure 5C, lane 1), *Pf*Mre11$^{F102C}$ did not form spontaneous disulfide bonds but could be linked by the disulfide bond promoter $Cu^{2+}$(Figure 5D). Using $Cu^{2+}$ we again tested the effect of ATPγS and found that disulfide bond formation is significantly reduced in the presence of ATPγS (Figure 5F).

To test whether ATP leads to a structure with increased DNA-binding affinity we used surface plasmon resonance (SPR) and electrophoretic mobility shift assays (EMSAs). Indeed, SPR showed a strong effect of AMPPNP on dsDNA and hairpin DNA binding by *Tm*Mre11:Rad50$^{NBD}$ (Figures 6A–6C; Figure S5A). Interestingly, the disulfide bonded *Tm*Mre11:Rad50$^{NBD,H830,D804C,F291S}$ complex showed even higher DNA affinity in the presence of AMPPNP, but we also observe some nonspecific interaction with the matrix, making the interpretation difficult (data not shown). For that reason we compared

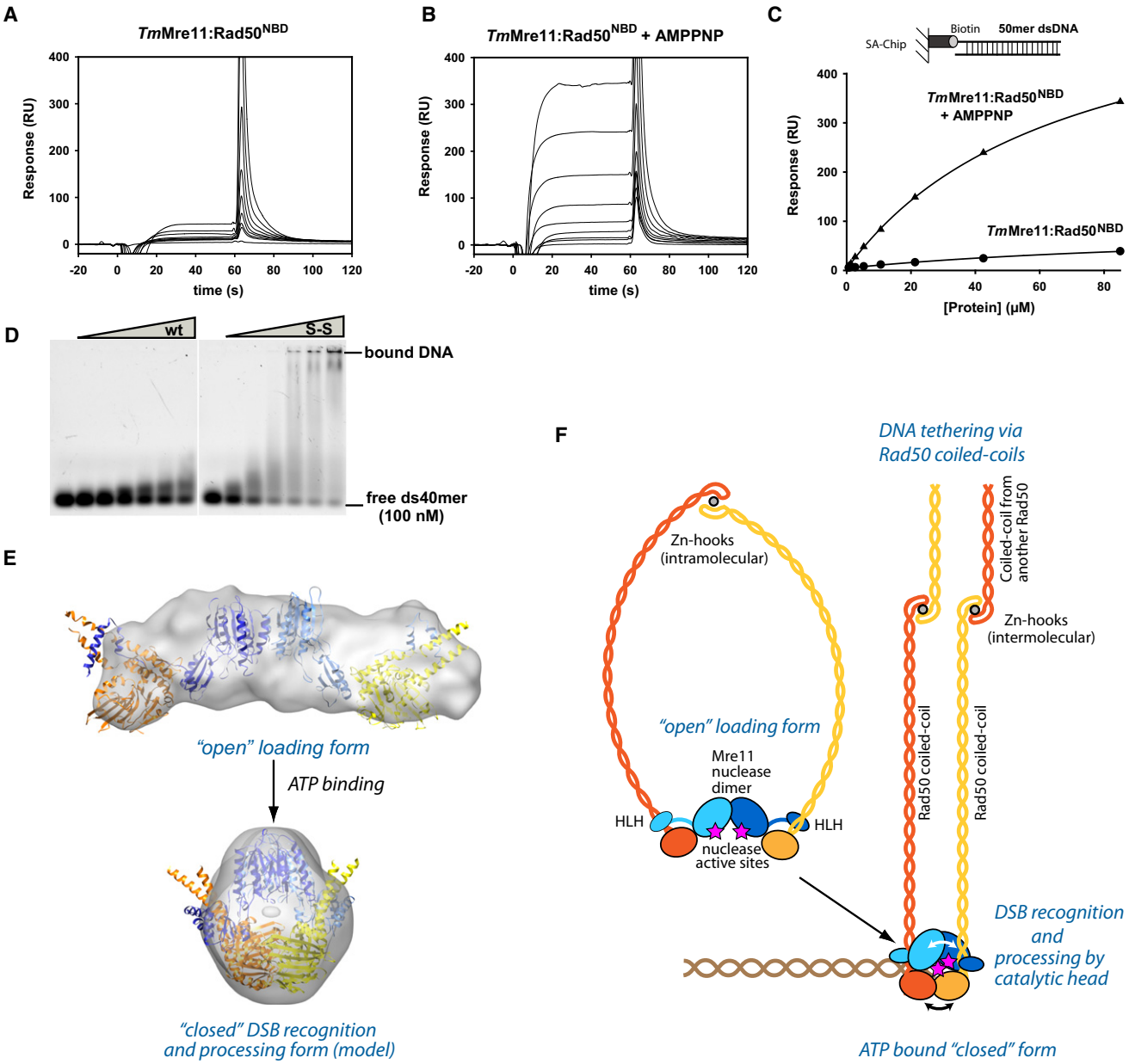


**Figure 6. ATP-Stimulated dsDNA Binding and Clamp Model for DSB Sensing**

(A and B) Surface Plasmon sensograms for binding of *Tm*Mre11:Rad50$^{NBD}$ to 50 mer dsDNA in absence (A) and presence of AMPPNP (B).

(C) Corresponding binding curves reveals AMPPNP-stimulated binding to dsDNA. AMPPNP also increases hairpin recognition (Figure S5A) and we also observe increased binding affinity of the protein with crosslinked Rad50 $^{NBD}$s (ATP mimic state) (data not shown).

(D) Electrophoretic mobility shift assays show that the MR$^{NBD,H830C,D804C}$ complex with a disulfide bond between the NBDs (S-S) has strongly increased dsDNA binding affinity compared to the wild-type MR$^{NBD}$ complex (WT). Following concentrations of the protein (0, 1.0, 2.5, 5.0, 7.5, 10.0, and 15.0 μM, respectively) were used.

(E) Model for the closed, clamp-like complex with engaged NBDs by combining X-ray structures and SAXS analysis. Open (experimental) and closed (rigid-body docked model) forms are displayed with corresponding SAXS envelopes.

(F) Proposed model for ATP-dependent DSB sensing and processing by MR by formation of a transient clamp at DNA end structures.

See also Figure S5.

*Tm*Mre11:Rad50$^{NBD}$ and *Tm*Mre11:Rad50$^{NBD,H830,D804C,F291S}$ also in EMSA and find a strongly increased binding of dsDNA oligonucleotides even in the absence of AMPPNP (Figure 6D). An EMSA using double-stranded plasmid ϕX174 RF II DNA verified the increased DNA binding of the MR$^{NBD}$ complex in the presence of AMPPNP and of the disulfide-bridged closed protein complex (S-S) (Figure S5B). These data suggest that the engaged, clamp-like form is the DNA-binding conformation.

### Implications for DSB Detection and ABC Enzyme Architecture

We provide here a structural framework for the architecture and ATP-dependent conformational changes of the bacterial MR complex. In the absence of ATP, the NBDs are widely separated, whereas ATP promotes a DNA-binding conformation by stabilizing an engaged form of the NBDs. Using SAXS data of the open and the 65% crosslinked form, we can generate ab initio reconstructions as well as rigid-body docked models of the ATP-bound, clamp-like structure (Figure 6E; Figures S5C–S5G and Extended Experimental Procedures for the SAXS analysis and modeling). The model is consistent with all crosslinking data as well as the high- and low-resolution structural data presented here. The structure draws interesting parallels to the Ku DNA end sensor, which forms a constitutive ring. This ring form makes Ku specific for DNA ends and prevents internal DNA binding (Walker et al., 2001). Other DNA-associated rings like PCNA or helicases are associated with ATP-dependent loading factors to allow encircling of DNA (Bowman et al., 2004). Our data suggest that MR forms a transient clamp, controlled by ATP binding. A proposed mechanism for DSB sensing is shown in Figure 6F. DNA-binding and nuclease-active sites are likely located in the central hole of the clamp, which might provide specificity for DNA end or hairpin structures, as in the case of Ku, but also allow controlled and limited DNA end processing by Mre11. In striking contrast to the constitutive ring shape of Ku, the open conformation of MR could explain how the complex can still bind to meiotic breaks with covalently attached Spo11.

The precise interaction of MR with DNA ends remains to be seen, but we were unable to detect crosslinked MR around plasmid DNA (Figures S3A–S3F). Additionally, we find that the crosslinked form can still bind to DNA ends that are blocked on both 5′ ends by a fluoresceine-specific single chain Fab antibody fragment (data not shown). It appears that the closed ATP-bound complex does not entrap dsDNA like, e.g., the PCNA ring and that ends are not simply recognized by a topological ring. This does not exclude the possibility that the open form of the MR complex can still bind to internal stretches of DNA. Indeed, a partially open form of the complex could bind to the DNA, diffusing along it to rapidly identify DSBs, where the NBD heads could fully engage in the presence of ATP to more strongly bind to DNA and, perhaps, melt and process ends (Figure 6).

Our finding, that ATP binding to Rad50 alters the crosslink sensitivity at the Mre11 dimer interface (Figures 5C–5F) and that the ATP-bound and/or crosslinked form of MR binds DNA much more tightly than the open form, draws an interesting parallel to the mechanism of the related ABC transporter ATPases. The possible explanation is that Rad50 promotes a structural change between the Mre11 protomers to induce a conformation with increased DNA-binding activity, but Rad50 contributes to DNA binding also directly in the presence of ATP (Hopfner et al., 2000; Raymond and Kleckner, 1993). Structural changes in Mre11 are appealing because they may not only provide a model for how ATP helps to trigger nuclease or DNA-melting activities of MR but also unify the functional architecture of MR with ABC transporters, where the conformational changes between the NBDs trigger conformational changes in TMDs to transport solutes (Hollenstein et al., 2007).

Biochemically, it has been found that some nuclease functions such as hairpin opening and ssDNA endonuclease activity do not require ATP, whereas others such as endonucleolytic cleavage of blocked DNA, dsDNA exonuclease, and 5′ dsDNA endonuclease require ATP (Paull and Gellert, 1998; Trujillo and Sung, 2001). It can be argued that latter activities might require partial melting of the DNA duplex to reach the active site of Mre11, and indeed MRN also possesses an ATP-stimulated dsDNA melting activity (Paull and Gellert, 1999). Given that Mre11 dimers cooperate to bind DNA and DNA is also bound across both Mre11 protomers (Williams et al., 2008), a structural modulation in the Mre11 dimer would be an ideal mechanism to provide the dsDNA melting activity and position DNA into the active site for endo/exonucleolytic cleavage.

In summary, we provide a structural framework for the architecture of the Mre11 Rad50 catalytic head module and reveal the ATP-dependent clamp formation responsible for DSB recognition and processing.

## EXPERIMENTAL PROCEDURES

### Proteins

*Tm*Rad50$^{NBD}$ was engineered by fusing N-terminal (residues 1–190) and C-terminal (residues 686–852) segments by an 8 amino acid linker (GGAGGAGG) in a single open reading frame, and coexpressed with *Tm*Mre11 (residues L7M–385). For crystallization of the AMPPNP Rad50$^{NBD}$ dimer, Rad50$^{NBD}$ was copurified with *Tm*Mre11 HLH (residues 343–385). Protein synthesis and purification procedures are provided in Extended Experimental Procedures.

### Crystallization and Structure Determination of the Mre11:Rad50$^{NBD}$ Complex

Crystals of *Tm*MR$^{NBD}$ were grown after mixing 2 μl of protein solution at 9.6 mg/ml protein concentration with 2 μl of the reservoir solution containing 9% (w/v) PEG-6000, 5% (v/v) MPD, 1 mM TCEP, and 0.1 M HEPES (pH 7.9). Prior to flash freezing in liquid nitrogen, crystals were transferred to reservoir solution supplemented with 10% (v/v) 2-methyl-2,4-pentanediole. Anomalous data to 3.4 Å were collected at the X06SA beamline (Swiss Light Source) on selenium-containing crystals. Details and statistics of data analysis and model building are provided in Extended Experimental Procedures.

### Crystallization and Structure Determination of the Mre11$^{HLH}$:Rad50$^{NBD}$:AMPPNP Complex

Crystals of *Tm*Mre11$^{HLH}$(aa 343–385):Rad50$^{NBD}$ were grown by mixing 200 nl of protein solution at 10.5 mg/ml protein concentration with 200 nl of the reservoir solution containing 20% (w/v) PEG-2000 MME, 0.2 M Trimethylamine N-oxide, and 0.1 M Tris (pH 8.5). Prior to flash freezing in liquid nitrogen, crystals were transferred to reservoir solution supplemented with 10% (v/v) 2,3-butandiol. Data to 1.9 Å were collected at the ID14-1 (European Synchrotron Radiation Facility). Details and statistics of data analysis and model building are provided in Extended Experimental Procedures.

### Small-Angle X-ray Scattering

SAXS data were acquired at the EMBL X33 beamline (Deutsches Elektronen-synchrotron) using a MAR345 two-dimensional image plate detector and at beamline BL12.3.1 (Advanced Light Source at Lawrence Berkeley National Laboratories). Scattering patterns were collected from solutions of *Tm*MR$^{NBD}$ in 50 mM Tris (pH 7.7), 100 mM NaCl, 5 mM $MnCl_2$, and 10 mM $MgCl_2$ at concentrations between 2 and 30 mg/ml. For details, see Extended Experimental Procedures.

### Crosslinking Analysis

Rad50 crosslinking reactions were performed either with MR$^{NBD,P31C,E806C}$ and HBVS (Pierce), MR$^{NBD,N64C,I760C}$, and BMOE (Pierce) or by formation of disulfide bonds (MR$^{NBD,H830,D804C,(F291S)}$). Crosslinking of the Mre11:Mre11

dimer was performed either by BMOE (Pierce) (*Pf*Mre11$^{F102C}$, *Tm*Mre11$^{S110C}$) or by formation of disulfide bonds with $Cu^{2+}$ (*Pf*Mre11$^{F102C}$). Details are provided in Extended Experimental Procedures.

### Cloning, Yeast Manipulation, and MMS Sensitivity Assays

The *MRE11* shuffle strain (Mat a; *his3Δ1*; *leu2Δ0*; *ura3Δ0*; *YMR224c::*kanMX4, pRS316-*MRE11*) was generated by transformation of the *MRE11/Δmre11* heterozygous knockout strain (Euroscarf) with pRS316-*MRE11*. Point mutations of *MRE11* were generated by quickchange site-directed mutagenesis of pRS313-*MRE11*. Plate survival assays of the *mre11* mutant strains were assessed by spotting 10-fold serial dilutions on SDC(–his) plates and SDC(–his) plates containing 0.005% MMS, 50 mM hydroxyurea or 1 μg/ml camptothecin. For detailed information, see Extended Experimental Procedures.

### DNA-Binding Analysis

DNA-binding reactions were carried out by SPR and EMSA. For detailed information, see Extended Experimental Procedures.

## ACCESSION NUMBERS

Atomic coordinates and structure factors have been deposited in the Protein Data Bank under accession codes 3QG5 for the Mre11:Rad50$^{NBD}$ complex and 3QF7 for the Mre11$^{HLH}$:Rad50$^{NBD}$:AMPPNP complex.

## SUPPLEMENTAL INFORMATION

Supplemental Information includes Extended Experimental Procedures, five figures, and two tables and can be found with this article online at doi:10.1016/j.cell.2011.02.038.

## ACKNOWLEDGMENTS

We thank John Petrini for his gift of an α-Mre11 antibody. We thank Britta Coordes for help with the yeast work and members of the Hopfner lab, especially Matthew Bennett, Gregor Witte, and Alfred Lammens, for discussions. We thank the staffs of the Swiss Light Source (Villingen), European Synchrotron Radiation Facility (Grenoble), German Electron Synchrotron (Hamburg), and Advanced Light Source (Berkeley) for technical support. We thank the Max-Planck-Crystallization Facility (Martinsried) for crystallization trials. This work was funded by grants from the German Research Council (SFBs 684, 646, and TR5), the German Excellence Initiative (CIPSM), European Commission (IP DNA repair), and NIH U19AI83025.

Received: June 28, 2010
Revised: December 22, 2010
Accepted: February 18, 2011
Published: March 31, 2011

## REFERENCES

Bentchikou, E., Servant, P., Coste, G., and Sommer, S. (2007). Additive effects of SbcCD and PolX deficiencies in the in vivo repair of DNA double-strand breaks in Deinococcus radiodurans. J. Bacteriol. *189*, 4784–4790.

Bhaskara, V., Dupre, A., Lengsfeld, B., Hopkins, B.B., Chan, A., Lee, J.H., Zhang, X., Gautier, J., Zakian, V., and Paull, T.T. (2007). Rad50 adenylate kinase activity regulates DNA tethering by Mre11/Rad50 complexes. Mol. Cell *25*, 647–661.

Borde, V. (2007). The multiple roles of the Mre11 complex for meiotic recombination. Chromosome Res. *15*, 551–563.

Bowman, G.D., O'Donnell, M., and Kuriyan, J. (2004). Structural analysis of a eukaryotic sliding DNA clamp-clamp loader complex. Nature *429*, 724–730.

Budd, M.E., and Campbell, J.L. (2009). Interplay of Mre11 nuclease with Dna2 plus Sgs1 in Rad51-dependent recombinational repair. PLoS ONE *4*, e4267.

Carney, J.P., Maser, R.S., Olivares, H., Davis, E.M., Le Beau, M., Yates, J.R., 3rd, Hays, L., Morgan, W.F., and Petrini, J.H. (1998). The hMre11/hRad50 protein complex and Nijmegen breakage syndrome: linkage of double-strand break repair to the cellular DNA damage response. Cell *93*, 477–486.

Chamankhah, M., and Xiao, W. (1999). Formation of the yeast Mre11-Rad50-Xrs2 complex is correlated with DNA repair and telomere maintenance. Nucleic Acids Res. *27*, 2072–2079.

Connelly, J.C., Kirkham, L.A., and Leach, D.R. (1998). The SbcCD nuclease of Escherichia coli is a structural maintenance of chromosomes (SMC) family protein that cleaves hairpin DNA. Proc. Natl. Acad. Sci. USA *95*, 7969–7974.

Connelly, J.C., de Leau, E.S., and Leach, D.R. (2003). Nucleolytic processing of a protein-bound DNA end by the E. coli SbcCD (MR) complex. DNA Repair (Amst.) *2*, 795–807.

Costanzo, V., Robertson, K., Bibikova, M., Kim, E., Grieco, D., Gottesman, M., Carroll, D., and Gautier, J. (2001). Mre11 protein complex prevents double-strand break accumulation during chromosomal DNA replication. Mol. Cell *8*, 137–147.

Cromie, G.A., Connelly, J.C., and Leach, D.R. (2001). Recombination at double-strand breaks and DNA ends: conserved mechanisms from phage to humans. Mol. Cell *8*, 1163–1174.

de Jager, M., van Noort, J., van Gent, D.C., Dekker, C., Kanaar, R., and Wyman, C. (2001). Human Rad50/Mre11 is a flexible complex that can tether DNA ends. Mol. Cell *8*, 1129–1135.

Eykelenboom, J.K., Blackwood, J.K., Okely, E., and Leach, D.R. (2008). SbcCD causes a double-strand break at a DNA palindrome in the Escherichia coli chromosome. Mol. Cell *29*, 644–651.

Harper, J.W., and Elledge, S.J. (2007). The DNA damage response: ten years after. Mol. Cell *28*, 739–745.

Hollenstein, K., Dawson, R.J., and Locher, K.P. (2007). Structure and mechanism of ABC transporter proteins. Curr. Opin. Struct. Biol. *17*, 412–418.

Hopfner, K.P., Karcher, A., Shin, D.S., Craig, L., Arthur, L.M., Carney, J.P., and Tainer, J.A. (2000). Structural biology of Rad50 ATPase: ATP-driven conformational control in DNA double-strand break repair and the ABC-ATPase superfamily. Cell *101*, 789–800.

Hopfner, K.P., Karcher, A., Craig, L., Woo, T.T., Carney, J.P., and Tainer, J.A. (2001). Structural biochemistry and interaction architecture of the DNA double-strand break repair Mre11 nuclease and Rad50-ATPase. Cell *105*, 473–485.

Hopfner, K.P., Craig, L., Moncalian, G., Zinkel, R.A., Usui, T., Owen, B.A., Karcher, A., Henderson, B., Bodmer, J.L., McMurray, C.T., et al. (2002). The Rad50 zinc-hook is a structure joining Mre11 complexes in DNA recombination and repair. Nature *418*, 562–566.

Hopkins, B.B., and Paull, T.T. (2008). The P. furiosus mre11/rad50 complex promotes 5′ strand resection at a DNA double-strand break. Cell *135*, 250–260.

Lavin, M.F. (2007). ATM and the Mre11 complex combine to recognize and signal DNA double-strand breaks. Oncogene *26*, 7749–7758.

Leach, D.R., Okely, E.A., and Pinder, D.J. (1997). Repair by recombination of DNA containing a palindromic sequence. Mol. Microbiol. *26*, 597–606.

Lee, J.H., and Paull, T.T. (2007). Activation and regulation of ATM kinase activity in response to DNA double-strand breaks. Oncogene *26*, 7741–7748.

Lee, K., Zhang, Y., and Lee, S.E. (2008). Saccharomyces cerevisiae ATM orthologue suppresses break-induced chromosome translocations. Nature *454*, 543–546.

Lobachev, K., Vitriol, E., Stemple, J., Resnick, M.A., and Bloom, K. (2004). Chromosome fragmentation after induction of a double-strand break is an active process prevented by the RMX repair complex. Curr. Biol. *14*, 2107–2112.

Lobachev, K.S., Gordenin, D.A., and Resnick, M.A. (2002). The Mre11 complex is required for repair of hairpin-capped double-strand breaks and prevention of chromosome rearrangements. Cell *108*, 183–193.

Mascarenhas, J., Sanchez, H., Tadesse, S., Kidane, D., Krisnamurthy, M., Alonso, J.C., and Graumann, P.L. (2006). Bacillus subtilis SbcC protein plays an important role in DNA inter-strand cross-link repair. BMC Mol. Biol. *7*, 20.

Mimitou, E.P., and Symington, L.S. (2008). Sae2, Exo1 and Sgs1 collaborate in DNA double-strand break processing. Nature *455*, 770–774.

Moreno-Herrero, F., de Jager, M., Dekker, N.H., Kanaar, R., Wyman, C., and Dekker, C. (2005). Mesoscale conformational changes in the DNA-repair complex Rad50/Mre11/Nbs1 upon binding DNA. Nature *437*, 440–443.

Neale, M.J., Pan, J., and Keeney, S. (2005). Endonucleolytic processing of covalent protein-linked DNA double-strand breaks. Nature *436*, 1053–1057.

Oldham, M.L., Davidson, A.L., and Chen, J. (2008). Structural insights into ABC transporter mechanism. Curr. Opin. Struct. Biol. *18*, 726–733.

Paull, T.T., and Gellert, M. (1998). The 3′ to 5′ exonuclease activity of Mre 11 facilitates repair of DNA double-strand breaks. Mol. Cell *1*, 969–979.

Paull, T.T., and Gellert, M. (1999). Nbs1 potentiates ATP-driven DNA unwinding and endonuclease cleavage by the Mre11/Rad50 complex. Genes Dev. *13*, 1276–1288.

Petrini, J.H. (2000). The Mre11 complex and ATM: collaborating to navigate S phase. Curr. Opin. Cell Biol. *12*, 293–296.

Putnam, C.D., Hayes, T.K., and Kolodner, R.D. (2009). Specific pathways prevent duplication-mediated genome rearrangements. Nature *460*, 984–989.

Raymond, W.E., and Kleckner, N. (1993). RAD50 protein of S.cerevisiae exhibits ATP-dependent DNA binding. Nucleic Acids Res. *21*, 3851–3856.

Sharples, G.J., and Leach, D.R. (1995). Structural and functional similarities between the SbcCD proteins of Escherichia coli and the RAD50 and MRE11 (RAD32) recombination and repair proteins of yeast. Mol. Microbiol. *17*, 1215–1217.

Stewart, G.S., Maser, R.S., Stankovic, T., Bressan, D.A., Kaplan, M.I., Jaspers, N.G., Raams, A., Byrd, P.J., Petrini, J.H., and Taylor, A.M. (1999). The DNA double-strand break repair gene hMRE11 is mutated in individuals with an ataxia-telangiectasia-like disorder. Cell *99*, 577–587.

Stracker, T.H., Theunissen, J.W., Morales, M., and Petrini, J.H. (2004). The Mre11 complex and the metabolism of chromosome breaks: the importance of communicating and holding things together. DNA Repair (Amst.) *3*, 845–854.

Trujillo, K.M., and Sung, P. (2001). DNA structure-specific nuclease activities in the Saccharomyces cerevisiae Rad50*Mre11 complex. J. Biol. Chem. *276*, 35458–35464.

Usui, T., Ohta, T., Oshiumi, H., Tomizawa, J., Ogawa, H., and Ogawa, T. (1998). Complex formation and functional versatility of Mre11 of budding yeast in recombination. Cell *95*, 705–716.

Varon, R., Vissinga, C., Platzer, M., Cerosaletti, K.M., Chrzanowska, K.H., Saar, K., Beckmann, G., Seemanova, E., Cooper, P.R., Nowak, N.J., et al. (1998). Nibrin, a novel DNA double-strand break repair protein, is mutated in Nijmegen breakage syndrome. Cell *93*, 467–476.

Walker, J.R., Corpina, R.A., and Goldberg, J. (2001). Structure of the Ku heterodimer bound to DNA and its implications for double-strand break repair. Nature *412*, 607–614.

Wang, J.H., Gostissa, M., Yan, C.T., Goff, P., Hickernell, T., Hansen, E., Difilippantonio, S., Wesemann, D.R., Zarrin, A.A., Rajewsky, K., et al. (2009). Mechanisms promoting translocations in editing and switching peripheral B cells. Nature *460*, 231–236.

Ward, J.F. (1988). DNA damage produced by ionizing radiation in mammalian cells: identities, mechanisms of formation, and reparability. Prog. Nucleic Acid Res. Mol. Biol. *35*, 95–125.

Williams, R.S., Williams, J.S., and Tainer, J.A. (2007). Mre11-Rad50-Nbs1 is a keystone complex connecting DNA repair machinery, double-strand break signaling, and the chromatin template. Biochem. Cell Biol. *85*, 509–520.

Williams, R.S., Moncalian, G., Williams, J.S., Yamada, Y., Limbo, O., Shin, D.S., Groocock, L.M., Cahill, D., Hitomi, C., Guenther, G., et al. (2008). Mre11 dimers coordinate DNA end bridging and nuclease processing in double-strand-break repair. Cell *135*, 97–109.

Zahradka, K., Buljubasic, M., Petranovic, M., and Zahradka, D. (2009). Roles of ExoI and SbcCD nucleases in "reckless" DNA degradation in recA mutants of Escherichia coli. J. Bacteriol. *191*, 1677–1687.

Zhu, Z., Chung, W.H., Shim, E.Y., Lee, S.E., and Ira, G. (2008). Sgs1 helicase and two nucleases Dna2 and Exo1 resect DNA double-strand break ends. Cell *134*, 981–994.